Communications Engineering

https://doi.org/10.1038/s44172-026-00618-3

Article in Press

X-ray fluorescence spectroscopy for rapid identification of cathode chemistry in lithium-ion battery recycling

Received: 11 April 2025

Accepted: 10 February 2026

Cite this article as: Ren, F., Vidal, V., Campos, A. *et al.* X-ray fluorescence spectroscopy for rapid identification of cathode chemistry in lithium-ion battery recycling. *Commun Eng* (2026). https://doi.org/10.1038/s44172-026-00618-3

Feihong Ren, Vladimir Vidal, Andréa Campos, Florence Vacandio, Bernard Angeletti, Isabelle Giffard, Perrine Chaurand, Daniel Borschneck, Suanto Syahputra, Jérôme Rose, Ismael Saadoune & Clément Levard

X-ray Fluorescence Spectroscopy for Rapid Identification of Cathode Chemistry in Lithium-ion Battery Recycling

Feihong Ren[1,3], Vladimir Vidal[1], Andréa Campos[2], Florence Vacandio[3], Bernard Angeletti[1], Isabelle Giffard[1], Perrine Chaurand[1], Daniel Borschneck[1], Suanto Syahputra[3], Jérôme Rose[1], Ismael Saadoune[4], Clément Levard[1,*]

Author affiliations :

1 Aix Marseille Univ, CNRS, IRD, INRAE, Coll France, CEREGE, Aix-en-Provence, France

2 Aix Marseille Univ, CNRS, Centrale Marseille, FSCM (FR1739), CP2M, 13397 Marseille, France

3 Aix Marseille Univ, CNRS, MADIREL (UMR 7246) and International Laboratory: Ionomer Materials for Energy, Campus St Jérôme, 13013 Marseille, France

4 Mohammed VI Polytechnic University (UM6P), Lot 660 – Hay Moulay Rachid, 43150 Benguerir, Morocco

Corresponding Author

*Clément Levard

E-mail: levard@cerege.fr ORCiD: 0000-0001-7507-7959

Abstract:

Efficient identification of cathode chemistry in end-of-life lithium-ion batteries is essential for enabling effective battery recycling. Current approaches often rely on battery disassembly or time-consuming testing, limiting their practical use at scale. Here we report a rapid classification strategy based on X-ray fluorescence spectroscopy combined with statistical analysis. A reference dataset was established from high-quality elemental spectra collected from more than 100 end-of-life lithium-ion batteries. Statistical grouping was used to define cathode categories, which were validated by selective disassembly and complementary chemical analysis. The trained classification model was then applied to newly acquired spectra collected within seconds per battery, enabling fast identification without additional disassembly. The approach achieves high prediction accuracy across the studied dataset and demonstrates the feasibility of rapid cathode identification for battery recycling applications.

Keywords: battery sorting, categorization, classification, cathode materials characterization, multivariate analysis

Introduction

The widespread adoption of lithium-ion batteries (LIBs) across sectors such as electric vehicles, portable electronics, and stationary energy storage systems has led to a dramatic increase in the number of spent batteries requiring efficient end-of-life (EOL) treatment[1–3]. As LIBs become a growing component of electronic and energy waste, the demand for sustainable and economically viable recycling strategies has intensified[4–6]. Cathode materials, in particular, are of major concern due to their content of critical and strategic metals, such as cobalt (Co), nickel (Ni), and manganese (Mn), which are essential to many current battery chemistries and valuable from a resource standpoint[7–11]. Conventional recycling technologies, including hydrometallurgical and pyrometallurgical processes, are capable of recovering these metals, but their efficiency and environmental impact depend strongly on the input material composition[12–15]. When cathodes of different chemistries are mixed, downstream purification becomes more complicated, often requiring intensive steps of more energy and reagents[16,17]. Therefore, the ability to sort EOL LIBs by cathode type prior to material recovery is crucial for improving process selectivity, reducing waste, and enhancing the economic feasibility of recycling.

Current LIB sorting approaches fall broadly into two categories: pre-disassembly and post-disassembly techniques[18]. Pre-disassembly methods often rely on external features, such as battery labels, form factors, or barcodes, to infer internal composition[19]. However, these indicators are frequently missing, misleading, or damaged, especially in second-hand or mixed waste streams. Electrochemical methods, including voltage profiling or impedance measurements, are used in some cases to assess battery state-of-health (SOH) or chemistry, but such tests are time-consuming and often require controlled conditions[20–22]. Post-disassembly methods such as inductively coupled plasma spectroscopy (ICP) can provide accurate cathode characterization, but they are

inherently destructive, labor-intensive, and impractical for high-throughput applications[23–25]. As a result, there remains a need for rapid, non-destructive, and scalable classification technologies that can operate directly on intact batteries.

X-ray fluorescence (XRF) spectroscopy is a promising candidate for such classification, as it offers elemental analysis and can, in principle, penetrate battery casings to detect internal cathode components[26], particularly when operated at higher excitation voltages. In this study, we used a benchtop XRF instrument operating at 50 kV, the typical maximum excitation voltage of most commercial XRF instruments, to evaluate the feasibility of cathode-based LIB classification under practical conditions. In previous studies, XRF has mainly been applied to analyze cathode materials after battery disassembly. In contrast, our work explored its application directly on intact EOL batteries for battery sorting. XRF offers a unique combination of speed, non-destructive analysis, and in-situ applicability, making it highly suitable for automated battery classification. Compared to destructive techniques like Inductively Coupled Plasma – Optical Emission Spectroscopy (ICP-OES) or Scanning Electron Microscopy – Energy Dispersive X-ray Spectroscopy (SEM-EDS), XRF provides a more efficient, scalable, and operationally simple solution for real-world LIB sorting in recycling workflows.

To explore the feasibility of classifying EOL LIBs based on cathode chemistry, we designed a multistep workflow that combines XRF spectroscopy with multivariate analysis. First, high-quality XRF spectra (5 minutes acquisition time) were collected from over 100 whole batteries and analyzed by principal component analysis (PCA) and hierarchical cluster analysis (HCA) to group the spectra according to their elemental signatures. To assign chemical meaning to these groups, a limited number of representative batteries were selectively disassembled and characterized by SEM-EDS and ICP-OES. The resulting compositions were used to label the XRF

groups and construct a reference dataset. Finally, a discriminant analysis (DA) model trained on this dataset was tested with newly acquired 5-second XRF spectra from the same battery groups. Within the studied sample set, the results suggest that short-duration XRF acquisitions can provide sufficient information for rapid, non-destructive classification of cathode types, although the approach may rely on both direct cathode signals and indirect signatures from casing or packaging materials. This XRF-based classification strategy may offer a practical foundation for real-time sorting of EOL LIBs by cathode type. By enabling identification without additional disassembly or characterization once the reference dataset has been established, it enables faster triage of EOL LIBs and better alignment of recycling streams. The methodology is compatible with automation, as the multivariate processing of XRF spectra can be implemented using programming languages, as demonstrated by the code provided in Supplementary Script 1. It could be integrated into LIB recycling facilities or waste-sorting infrastructures to improve metal recovery efficiency and reduce environmental burden. It should be noted that the present study focuses on demonstrating the feasibility of XRF-based classification. The specific battery groups observed reflect the distribution of commercial EOL batteries available in our dataset, and other cathode–cell format combinations may exist in different contexts.

Results and Discussion

Battery samples and exploration of XRF experimental conditions

The samples used in this work were 108 EOL LIBs collected from the recycling center of a battery retailer (1001 PILES BATTERIES) based in France. Their brands, shapes, and types were selected randomly. Based on their shape, batteries can be categorized as pouch batteries (44 units), coin cells (15 units), and cylindrical batteries (49 units). Figure 1a-c show optical photos with the corresponding X-ray transmission (XRT) images. Understanding the internal structure of the

battery can help determine the optimal conditions for XRF analysis. XRT images can reveal the internal structure of a battery without disassembly. As shown in the XRT images in Figure 1a, at the bottom of the pouch cell there is a circuit board that functions as a battery management system (BMS) to protect the battery; the majority of the shadowed area was assumed to be the electrode sheets, and the darker area on the left is probably the electrical tab that connects the internal and external electrodes. Figure 1b shows that there is a net structure in the central electrode area of the coin cell, which likely serves as a support or a current collector for the electrode. The front view of the XRT image in Figure 1c reveals that, apart from the top cap, the shaded areas represent electrodes. The spiral shape visible in the bottom view further indicates that the electrode sheets are rolled up inside the casing (Supplementary Figure 13). To verify the chemical homogeneity of the battery, Figure 1d compares the XRF spectra at various points on a pouch cell. The shape, position, and intensity of the peaks of these spectra are quite similar, indicating that the chemical composition is uniform throughout the battery. Accordingly, five different points were chosen on the batteries for the XRF test, excluding areas near the edges of the casing (Supplementary Figure 1). To obtain a high-quality spectrum, 5 min of acquisition time was used for each point.

Classification and validation of XRF spectra from intact batteries by multivariate statistics

The normalized XRF spectra of the intact 108 spent batteries are shown in Figure 2a (The spectra were normalized by Rh element's $K_{\alpha 1}$ peak inherent to the X-ray source). It is well known that five types of cathode materials are currently used in commercial lithium-ion batteries: $LiMn_2O_4$, $LiCoO_2$, $LiNi_xCo_yMn_zO_2$, $LiNi_xCo_yAl_zO2$, and $LiFePO_4$[27]. Due to the low emission energy of lithium, it is difficult to detect using XRF, and since Li is commonly found in cathode materials, the main metallic elements to be investigated in this work are Al, Mn, Fe, Co, and Ni. The peak intensities in the XRF spectra are positively correlated with the concentration of the elements.

Therefore, establishing the relationship between the XRF peak intensities of these five elements and the types of cathode materials is the key to sorting the batteries. The intensities corresponding X-ray emission energy ($K_{\alpha 1}$) of the five elements, here considered as five variables, can be studied by multivariate statistical analysis. To reduce the number of variables and extract the most important information, PCA can be used to reduce data dimensionality, which will also simplify subsequent calculations. In the PCA scree plot (Figure 2b), an elbow point appears at PC2, meaning that together, PC1 and PC2 explain 71.6% of variance. Hence, by projecting the original data onto a new coordinate system using linear transformation, the projected data has the maximum variance along these two dimensions, as shown in the PCA biplot (Figure 2c), thereby highlighting the main information in these dimensions. To further classify the batteries based on the PCA-dimensionality-reduced data (data represented by PC1 and PC2), HCA can be used to group the intact batteries into different categories according to similar chemical information derived from their XRF spectra, progressively clustering them to form a hierarchical structure, thereby constructing a tree-like "cluster dendrogram" (Figure 3a). Since HCA calculates the similarity between data objects through a distance metric, in this case, cutting the dendrogram at a distance of 1.25 resulted in 5 groups: A, B, C, D and E identified by different colors in the Figure 3a. Group A consists of coin cells, Groups B and C are pouch cells, Groups D and E are cylindrical cells, as confirmed by visual inspection. The clustering results of HCA can be combined with the results of PCA to obtain groups labeled by different colors, along with 95% confidence ellipses (Figure 3b). It shows that the distances between the groups are relatively large, even though Groups B, C, and E have a small overlap, indicating clear differences between the samples of each group. Group C contains a higher amount of Co, Groups B and E contain more Mn, while Groups D and A are rich in Ni, Al, Fe, and Mn. This is just a preliminary observation, since the intensities corresponding to the emission energy of elements are used here, whereas there may be cases of

peak overlap and masking, therefore, the detailed XRF spectra require further discussion. Assuming the groups resulting from HCA can successfully classify batteries according to the types of cathode materials, then when new XRF spectra data of samples are obtained, DA can be used to predict the group to which the new data will be assigned. In DA, each spectrum is projected onto discriminant functions that maximize the separation between the predefined groups, and the assignment is determined by the group with the highest post probability (P_{max}; see Supplementary Methods: Calculation of post probabilities in discriminant analysis), which quantifies how likely the sample belongs to each group based on its multivariate elemental signature. Thus, three batteries (battery code: battery group + 1, 2, 3) were randomly selected from each of the five groups to re-acquire XRF spectra, and these data were acquired using the XRF spectrometer's minimum acquisition time (5 seconds) to validate that spectra data with rapid acquisition is enough for sorting batteries, that is to say, a short acquisition time for the measurement of fluorescence spectra was chosen with a view to on-line sorting. However, the X-ray source used for this study is not suitable for optimizing this acquisition time, given its low flux compared with the latest generation of X-ray sources. As shown in Supplementary Figure 14, despite higher noise compared to 5min spectra, 5 s spectra preserve the characteristic peaks and relative intensities, confirming their adequacy for DA-based identification. The DA method was then applied to predict whether they could be accurately categorized to the correct groups. Supplementary Figure 2 shows the intensity of the corresponding $K_{\alpha 1}$ of the five elements (Al, Mn, Fe, Co, Ni) used as variables, the group results of HCA served as categories, the discriminant function plot conducted on 108 batteries. In the direction of the two discriminant functions, *F*1 and *F*2, the original data exhibits the optimal projection direction for classifying the categories after linear transformation, and the large degree of dispersion between groups indicates that it is easier to distinguish between them. Supplementary Table 11 lists the post probabilities of XRF data with a 5-second acquisition time for each group,

allowing the prediction of the battery groups. Furthermore, Table 1 summarizes representative battery samples from each group, showing the cell type, the main metallic elements detected (with their $K_{\alpha 1}$ energies), the DA prediction, the corresponding P_{max}, and the corresponding cathode chemistry confirmed by subsequent complementary destructive analysis. All group prediction results are correct, with P_{max} for their corresponding correct groups exceeding 99%. To simplify and accelerate multivariate analysis through automated computations, all three types of multivariate analysis (PCA, HCA, DA) can be implemented using code programming. For example, using R language to process XRF data for sorting batteries is provided in Supplementary Script 1.

XRF analysis of intact batteries and battery components

The goal of classifying and sorting EOL LIBs using chemical information from XRF data of intact batteries was thus achieved. It should be emphasized, however, that this chemical information inevitably includes strong contributions from casing and packaging materials, while the extent to which signals from the internal components—especially the cathode—are detected remains uncertain. Based on x-ray transmission calculations (see Supplementary Methods: Calculation of the transmission (T) of X-rays through a casing or packaging), the 50 kV X-ray source provides sufficient excitation of cathode fluorescence inner battery (Supplementary Table 1), and while fluorescent X-rays (Supplementary Table 2) readily escape through Al-casing pouch casings (Supplementary Table 3), they are strongly attenuated by stainless-steel casings of coin (Supplementary Table 4) cells and cylindrical (Supplementary Table 5) cells. Although this first objective has been achieved, analysis of the intact battery without dismantling only provides partial information on the true composition of the cathode. In particular, the nature of the casing or packaging can severely limit identification of the cathode type. Figure 4 shows the XRF spectra

of the intact batteries for the five groups. Compared to Groups A, D, and E, Groups B and C (pouch cells) exhibit more diverse information concerning the elements, suggesting that XRF can detect chemical information inside the battery. For instance, Cu may come from the current collector in the anode [28], Si from the protective coating (SiO_2) on the separator [29], and Cl from the lithium salt ($LiClO_4$) or additives in the electrolyte [30]. The casings of coin cells (Group A) and cylindrical cells (Groups D and E) are usually made of stainless steel, so elements like Fe, Ni, and Cr are likely to come from the metal casing of the batteries. The casings of pouch cells (Groups B and C) are usually made of Al alloy, which has a low atomic density, meaning X-ray may easily penetrate and limit secondary X-ray emissions absorption compared to stainless steel. Indeed, the stainless-steel casing of cylindrical cells has a high atomic density, causing strong attenuation of X-rays as they pass through. Additionally, the stainless steel itself generates strong characteristic X-ray fluorescence that may obscure weaker fluorescence signals coming from inside the battery.

Although our classification method is designed to operate on intact EOL batteries, the true cathode compositions of the collected samples were initially unknown, as most batteries lacked comprehensive labeling or documentation regarding their cathode chemistry. Therefore, to establish a reliable reference dataset and validate the classification results obtained from intact-battery XRF analysis, three representative batteries were selected from each group and disassembled for further characterization. The components of the disassembled batteries are shown in Supplementary Figure 3. As illustrated in Supplementary Figure 3a, there is noticeable yellow powder on the separator and negative casing of the coin cell. When the negative casing is immersed in water, it produced many bubbles (Supplementary Figure 3b-c), suggesting the presence of Li metal as anode, while cathode material is a black, self-supporting bulk, indicating that it is most likely a typical Li/MnO_2 primary coin cell. XRF spectra can be used to check this assumption later.

As shown in Supplementary Figure 3d and f, the pouch and cylindrical cells contain a cathode sheet, an anode sheet, and two separators, all of which are rolled up inside the metal casing (Supplementary Figure 3e and g). Typically, the outermost layer is the cathode sheet or the cathode sheet covered by the separator, which helps XRF detect chemical information about the cathode material before the battery is disassembled. The XRF spectra of the different components of the batteries are shown in Figure 5 (comparison of cathode materials and intact batteries), Supplementary Figure 4 (metal casings), Supplementary Figure 5 (separators), and Supplementary Figure 6 (plastic packaging). Supplementary Table 12 summarizes the metals and their $K_{\alpha 1}$ signals detected from intact batteries, metal casings, plastic packaging and cathodes across different cell formats. The coin cells in Group A have no plastic packaging, while the plastic packaging and metal casing are integrated in Group C. In Group A (coin cells), the intact battery and metal casings are nearly identical, and contain elements Cr, Fe, and Ni, which are the fundamental components of stainless steel. The Mn in the separator of Group A originates from the cathode material, Cl comes from the electrolyte, and Ca may come from the protective coating ($Ca(OH)_2$) on the separator [31]. In the cathode materials of Group A, only Mn was detected, aside from a small amount of Cl, which may originate from the electrolyte. The Cr element's $K_{\beta 1}$ and Fe element's $K_{\alpha 1}$ signals from the metal casing probably obscure the Mn element's $K_{\alpha 1}$ and $K_{\beta 1}$ signals in the cathode material respectively, making it difficult to detect the chemical information inside the battery. The cathode materials in Group B (pouch cells) contain relatively diverse elements, and Mn, Co, and Ni were detected. The metal casings in Group B consisted of an Al alloy containing Al, Cl, Mn, Fe, and Cu. The P and Cl in Group B's separator likely originate from the electrolyte, while Al may originate from the cathode's current collector. Cl and Ti were found in the plastic packaging used in Group B, possibly derived from polyvinyl chloride (PVC) and a TiO_2 additive, respectively. Although Mn in the cathode materials of Group B was detected in the XRF spectrum of the intact

battery, Mn was also present in the metal casing. Furthermore, the Mn-$K_{\alpha 1}$ and Fe-$K_{\alpha 1}$ peak height ratios resembled the spectra of both the intact battery and of the metal casing, meaning that, unless the battery is disassembled, XRF is unlikely to provide reliable chemical information about the cathode materials inside the batteries in Group B. Although both Group B and Group C correspond to pouch cells, their casings are not identical. Elemental analysis of the foils (Supplementary Figure 4) showed that the Group B casing contains Mn, which strongly attenuates fluorescence signals in the 6–8 keV range. As a result, Co and Ni peaks are not visible in the Group B spectra, even though these elements are present in the cathode composition confirmed by dismantling, while in Group C the thin and Mn-free foil allows Co fluorescence to be detected. Ti, Cl, Fe, and Ni were detected in the XRF spectra of the intact batteries in groups D and E (cylindrical cells). Ti and Cl originated from the plastic packaging, while Fe and Ni originated from the stainless-steel casing. P, Cl, and S were found in the separators of groups D and E. Mn, Co, and Ni were detected in the cathode materials of all the other samples in groups D and E except for sample E-2, in which only Mn was detected in the cathode material. As shown in Supplementary Figure 6, the plastic packaging within groups D or E is similar; notably, group D exhibits little Cl whereas group E shows pronounced Cl signals. The metal casings of groups D and E are also comparable (Supplementary Figure 4), yielding similar Fe–Ni features when measured alone. In the intact battery spectra (Figure 5), sample D-2 still displays Ni $K_{\alpha 1}$ higher than Fe $K_{\alpha 1}$ even though its casing-only spectrum shows Fe $K_{\alpha 1}$ > Ni $K_{\alpha 1}$ and its plastic packaging contains negligible Cl. This indicates that, when Cl-induced attenuation is negligible, we interpret this reversal as evidence that the intact-battery Ni $K_{\alpha 1}$ is enhanced by an additional cathode contribution, enabling inference about internal Ni without disassembly. By contrast, in group E the Cl-rich plastic packaging can skew the apparent Fe/Ni ratio via differential attenuation: for a typical PVC thickness of 80–100 μm, our calculation gives an Ni-to-Fe transmission of ~1.6–1.8× (Supplementary Tables 6 and 7),

meaning Fe $K_{\alpha 1}$ is preferentially suppressed relative to Ni $K_{\alpha 1}$. Therefore, Fe—originating from the stainless-steel casing—is not used as an internal reference for cathode composition, and Ni-related interpretations for group E are made with caution. Where required, removing the outer plastic wrap (without opening the metal can) can further improve Ni assessment for cylindrical cells.

Validation of cathode compositions by analyses of dismantled batteries

Supplementary Figure 7 shows the results of the semi-quantitative XRF analysis of the cathode material. Since the fluorescent X-ray emission energy of Li is too low to be detected by XRF, further quantitative analysis of the cathode material was conducted using ICP-OES (Figure 6). ICP-OES is more sensitive than XRF, with a lower detection limit, and thus provides more accurate quantitative results. Apart from Li, the ratios of the amounts of the elements were consistent in the XRF and the ICP-OES results, further confirming the accuracy of the XRF analysis. The concentration of Al in each sample was extremely low or even zero, suggesting that Al may not originate from the cathode material but from the shedding or high-voltage decomposition of Al current collectors. Even though these samples were fully discharged before ICP-OES analysis, lithium ions may not have been completely intercalated into the lattice of the cathode material due to battery degradation, resulting in a discrepancy in the ratio of lithium ions to other metal ions compared to that of a brand-new battery. In group C, the concentration of Li was similar than that of Co, with a ratio of approximately 1:1, strongly suggesting the cathode material is $LiCoO_2$. The concentration of Li in the three group A samples varied, perhaps because the MnO_2 cathode can be discharged to form Li_xMnO_2. The cathode materials in groups B, D, and E primarily contained the three transition metals Ni, Co, and Mn. In particular, the ratio of Li to Mn in sample E-2 was approximately 1:2, suggesting it could be $LiMn_2O_4$. Although the presence of Ni, Co, and Mn as

transition metals may indicate $LiNi_xCo_yMn_zO_2$, the concentration of Ni in $LiNi_xCo_yMn_zO_2$ in the commercial field is generally higher than or equal to that of Co and Mn. Therefore, the cathode materials in samples B-1, B-2, B-3, E-1, and E-3 may consist of more than one type, potentially a mixture of $LiNi_xCo_yMn_zO_2$ with $LiCoO_2$ or/and $LiMn_2O_4$. More detailed information concerning the types of cathode materials was obtained through SEM-EDS analysis. The morphology of the cathode materials can reveal their type. For example, the bulk-like morphology in Supplementary Figure 8a corresponds to the MnO_2 electrode (Sample A-2) in the Li-MnO_2 primary cell [32], the compact layered structure of micron-sized particles in Supplementary Figure 8b (Sample C-1) correspond to $LiCoO_2$ [33], the irregular shaped aggregate or agglomerate of primary sub-micron and micron-sized particles in Supplementary Figure 8c (Sample E-2) correspond to $LiMn_2O_4$ [34], and the spherical aggregate or agglomerate of primary sub-micron particles in Supplementary Figure 8d (Sample D-1) correspond to the typical morphology of $LiNi_xCo_yMn_zO_2$ [35]. Figure 7 shows the SEM-EDS mapping images of 15 samples from 5 groups. When combined with the results of ICP-OES analysis, the types of their cathode materials can be inferred. Group A consisted entirely of Li_xMnO_2; in Group B, samples B-1 and B-2 were mixtures of $LiCoO_2$ and $LiNi_xCo_yMn_zO_2$, while B-3 contained a mixture of $LiCoO_2$, $LiMn_2O_4$, and $LiNi_xCo_yMn_zO_2$. In Group C, aside from a few Al particles, the samples were mainly composed of $LiCoO_2$. In Group D, samples D-1 and D-2 contained $LiNi_xCo_yMn_zO_2$, while D-3 was a mixture of $LiNi_xCo_yMn_zO_2$ and $LiMn_2O_4$. Group E samples were mixtures of $LiNi_xCo_yMn_zO_2$ and $LiMn_2O_4$, but $LiNi_xCo_yMn_zO_2$ particles were rare in E-2. Next, the phase identification of the cathode material was analyzed by XRD, providing further evidence needed to identity the types of cathode materials. In the XRD spectrum of Group A, signals were mostly obscured by noise (Supplementary Figure 9a), suggesting that this material is amorphous. The XRD spectra of Groups B-E (Supplementary Figure 9b) were mainly consistent with the results of SEM-EDS. Co_3O_4 was detected in some spectra, showing that an irreversible

side reaction can occur in extreme conditions, such as when the cathode material undergoes overcharging or degradation of its structure due to overlong utilization. This also explains the slight shifts in the positions of the peaks observed in certain spectra. These destructive analyses, which involved physically disassembling a limited number of representative batteries, were conducted solely during the development phase to validate the classification model. The results confirmed that the grouping derived from intact-battery XRF analysis accurately reflects the underlying cathode compositions, thereby supporting the effectiveness of the proposed non-destructive method in real-world applications without further disassembly.

Hence, by using XRF technology combined with multivariate analysis, spent batteries were classified in five groups: one group of coin cells, two groups of pouch cells, and the other two groups of cylindrical cells. In our sample set, the cathode material of the coin cells was primarily Li-MnO_2. For pouch cells, one type used $LiCoO_2$ as the cathode, while the other used a combination of at least two materials out of three: $LiCoO_2$, $LiMn_2O_4$ and $LiNi_xCo_yMn_zO_2$. The cathode material in cylindrical batteries was a mixture of $LiNi_xCo_yMn_zO_2$ and $LiMn_2O_4$, one type had low Ni contents and another had high Ni contents (Figure 6b). Interestingly, we also observed an empirical correlation between packaging configuration and cathode chemistry. Cells with separable sleeves (Group B) were more often associated with mixed transition-metal cathodes ($LiNi_xCo_yMn_zO_2$), while cells with integrated plastic/Al casings (Group C) were more frequently $LiCoO_2$-based. This tendency may reflect an evolution of battery technology, in which newer Ni-rich $LiNi_xCo_yMn_zO_2$ cathode are equipped with reinforced packaging for improved safety. For instance, Ca was detected in the plastic packing of Group B (Fig. S6), likely introduced as a flame-retardant additive, while Mn and Cu were found in the metal casing, possibly to increase mechanical strength. These observations highlight the interplay between cathode chemistry and

packaging design in modern pouch cells, although the correlation should not be considered universal. Similarly, Groups D and E of cylindrical cells also showed differences in their packaging-related signals. Group E exhibited strong Cl fluorescence, which is probably consistent with PVC-based shrink sleeves, whereas Group D showed only weak Cl but stronger Ti signals, likely arising from non-chlorinated poly(ethylene terephthalate) (PET) or polyolefin sleeves sleeves pigmented with TiO_2. Within our sample set, Group D cells more frequently contained high content of $LiNi_xCo_yMn_zO_2$ cathodes, while Group E cells did so less often. This trend may again reflect technological and regulatory evolution: the widespread adoption of Ni-rich $LiNi_xCo_yMn_zO_2$ chemistries coincided with a shift from chlorinated to halogen-free sleeves, driven both by safety considerations and environmental regulations. As in the case of Groups B and C, however, this correlation should be regarded as sample-specific rather than universal. These observations, including the apparent correlations between packaging configuration and cathode chemistry in both pouch and cylindrical cells, should be understood as sample-specific and may not be generalizable beyond the regional battery stock sampled in this study. For clarity, Figure 8 summarizes the overall XRF-based classification strategy developed in this study.

XRF vs. electrochemical methods for cathode identification

We compared this approach with the electrochemical method to identify cathode materials in batteries. Obtaining stable and effective electrochemical data for batteries often requires long testing times (e.g., a few days). For example, as shown in Supplementary Figure 10, obtaining discharge-charge curves for batteries requires low-current testing at 0.1 C. (Note that in group A, coin cells cannot be recharged and only have discharge curves; further discharge is impossible for A-1 and A-2 due to full depletion of capacity.) Under these conditions, testing three cycles would take approximately 60 hours, which is considerably longer than the time required by XRF.

Although SOH (state of health= the maximum charge capacity available of battery/the nominal capacity ×100%) testing is needed by industry for cascade utilization of EOL LIBs, such testing usually targets battery packs rather than individual cells due to time constraints and economic value. Furthermore, if the SOH is below 20%, the battery is no longer suitable for cascade utilization, so confirmation of the elemental composition is necessary. Supplementary Figure 11 shows the SOH of the batteries used in this study. Except for the coin cells in group A, which had an SOH < 20%, the SOH in all other groups were > 20%, and some even higher than 90%. This is due to the low-current testing we used; we expect that testing at a 1C rate (fully charging the battery in 1 hour, which is more practical in daily life, like for smartphones) would result in a substantial reduction in SOH. Mathematical transformations of the charge-discharge curves produced the dQ/dV curves (Supplementary Figure 12) that represent the change in charge resulting from a change in unit voltage at a specific voltage. Each peak on the curve typically corresponds to an electrochemical reaction. Even for the same material, the dQ/dV peak values can fluctuate across different cycles, making it less accurate than XRF. Even if the shape of the curve suggests the type of cathode material, such as the typical $LiCoO_2$ curve seen in Group C [36], only the characteristic $LiNi_xCo_yMn_zO_2$ curve was observed in B-3 [37]. This may be due to the minimal contribution of $LiCoO_2$ and $LiMn_2O_4$ to the charge-discharge process, which causes their signals to be obscured. Therefore, using XRF technology for the identification and classification of cathode materials in EOL LIBs offers advantages in terms of both speed and accuracy.

Perspectives for real-time battery sorting by XRF

Although no $LiFePO_4$ cells were encountered in the collected sample set, XRF is in principle applicable to $LiFePO_4$. Transmission calculations indicate that in pouch formats (Supplementary Table 8), Fe $K_{\alpha 1}$ (~83%) and even P $K_{\alpha 1}$ (~49%) can be detected, enabling $LiFePO_4$ identification

via Fe together with the absence of Ni/Co; in contrast, in steel-cased formats (Supplementary Tables 9 and 10), Fe $K_{\alpha 1}$ transmission drops below 0.01% and P $K_{\alpha 1}$ is essentially fully absorbed, making non-destructive detection intrinsically very difficult. Such cases would require confirmatory destructive testing. In an inline setting, a single short XRF acquisition can read casing/packaging chemistry and—where fluorescence escape permits—extract cathode signatures from Mn/Fe/Co/Ni $K_{\alpha 1}$ ($\approx$ 5.9–7.5 keV). Our benchtop study used 50 kV (Si detector) and the minimum acquisition time was 5 s per spectrum; with higher-flux sources, large-area or multi-head detectors, and optimized geometry/filters, equivalent Signal-to-Noise Ratio is realistically achievable in ~1–2 s (counts $\propto$ flux × solid angle × time). For Al-casing pouch cells, 40–50 kV is appropriate to excite the relevant K lines and support short dwell provided the casing contains not too much heavy-element-rich. For steel-cased coin/cylindrical cells (~0.25–0.30 mm stainless steel), the emitted cathode K_{α} photons remain at 6–8 keV and are strongly absorbed, so direct through-steel identification in 1–2 s is generally unreliable at typical wall thicknesses. Nevertheless, XRF still enables non-destructive triage via casing/packaging chemical elements (e.g., Fe/Ni steel; Cl-bearing PVC vs Ti-pigmented halogen-free sleeves; Mn-bearing Al laminates), which in our sample set showed non-universal correlations with cathode choices. Importantly, a 140 kV x-ray source with CdTe (Supplementary Figure 15) proof-of-concept on a pouch cell with an Mn-bearing Al casing (Group B) reduced metal casing peaks and improved the relative visibility of Mn and Co $K_{\alpha 1}$ that were masked at 50 kV (Supplementary Figure 16), indicating that harder, high-flux excitation can mitigate casing/laminate masking; by analogy, $\geqslant$ 120–140 kV with CdTe/Ge detection and larger solid angle may retrieve weak but classifiable cathode cues in steel formats without opening. Together, these considerations outline a practical,

non-destructive pathway to real-time sorting that leverages direct cathode fluorescence whenever available and relies on packaging-related signatures when cathode emission is not accessible.

Conclusion

In this work we demonstrate the feasibility of rapidly classifying cathode chemistries in end-of-life LIBs non-destructively by benchtop XRF combined with multivariate analysis. Using a 50 kV source and 5 s acquisition, the method provides actionable chemical signatures without further disassembly; acquisition times could be further shortened with higher-flux spectrometers. Importantly, the XRF signatures we use reflect both the internal cathode and the external materials (metal casing and plastic packaging), and internal cathode peaks are not always detectable—especially for dense or thick casings and Cl-rich plastic packaging where attenuation is strong. Within our dataset, five operational groups were distinguished after explicitly considering packaging/casing effects: coin cells predominantly showed Li–MnO_2; pouch cells were either $LiCoO_2$ or blends involving at least two among $LiCoO_2$, $LiMn_2O_4$, and $LiNi_xCo_yMn_zO_2$; cylindrical cells formed two subgroups whose intact-battery spectra were consistent with $LiNi_xCo_yMn_zO_2$-type chemistries exhibiting comparatively lower or higher Ni signatures, with possible co-presence of $LiMn_2O_4$ in some samples. Notably, for Al pouch cells we could separate a pure $LiCoO_2$ group without disassembly, which is operationally valuable for directing Co-rich streams to appropriate recovery routes. These assignments were corroborated by post-mortem analyses on the same samples (Figures 5–7), but they reflect this dataset only and are not intended to represent the full space of format–chemistry combinations found in the market. Overall, this exploratory workflow offers a practical path to triage EOL cells and improve recycling logistics—especially for cobalt- and manganese-bearing streams—while minimizing processing time and environmental burden.

Methods

Materials

A total of 108 spent lithium-ion batteries were collected from 1001 PILES BATTERIES (Aix-en-Provence, France). The sample set comprised 44 pouch cells, 15 coin cells, and 49 cylindrical cells. Only 18650 cylindrical cells were included, while several types of coin cells were used: CR2460, CR2016, CR2025, CR2032, and CR2032H. The pouch cells were sourced from spent batteries of different brands of mobile phones. Prior to disassembly, all batteries were fully discharged for safety reasons.

Experimental procedures

Battery disassembly was carried out under a fume hood. To obtain cathode powders for chemical analysis, cathode sheets were first heated at 580 °C for 10 min in a muffle furnace to remove the polyvinylidene fluoride (PVDF) binder, enabling separation from the aluminum current collector. Subsequently, the samples were subjected to 630 °C for 6 h to eliminate conductive carbon black. To prepare the digested solutions for ICP-OES analysis, approximately 50 mg of cathode powder was sequentially digested with 2 mL HNO_3 (69%), 2 mL HCl (37%), and 0.5 mL HF (40%) (all trace metal grade). The resulting solutions were diluted with ultrapure water (18.2 MΩ·cm at 25 °C) to a final dilution factor of 200.

Characterization

X-ray fluorescence (XRF) spectra were acquired using a HORIBA XGT-7000 microscope equipped with a Rh target and a high-purity Si detector. Measurements were performed at 50 kV with a 100 μm beam size. To obtain high-quality spectra, the acquisition time was 5 min, and each sample was measured at least three times. To rapidly sort a battery by XRF with discriminant

analysis (DA), the acquisition time was then decreased to 5 s (minimum value of the machine). XRF spectra were normalized using the Rh $K\alpha_1$ fluorescent peak inherent to the X-ray source. Electrochemical performance was assessed by subjecting battery samples to three charge/discharge cycles at 0.1C/0.1C in the voltage range of 2.6–4.2 V, using a multichannel potentiostat (BioLogic, VMP3). Surface morphology was investigated by scanning electron microscopy (SEM, Zeiss GeminiSEM 500) operated at 15 kV, coupled with an EDAX Octane Silicon Drift Detector (129 eV energy resolution for Mn) for elemental mapping (EDS). Phase identification was conducted using X-ray diffraction (XRD, PANalytical X'Pert PRO MPD) with Co Kα radiation ($\lambda = 1.7928$ Å), scanned from 10° to 90° at a step size of 0.02° s^{-1}. The elemental composition of the cathode materials was analyzed by ICP–OES (PerkinElmer Optima 4300 DV) on the digested solutions (preparation protocol in experimental section) of cathode powders. High energy XRF was carried out in a micro-CT system (Zeiss MicroXCT-400, maximum tube voltage 140 kV) coupled with a CdTe detector (HEXITEC Gige, Quantum detectors).

Statistical analysis

Multivariate analysis was conducted under the module Statistics by Origin Pro 2021. The R script was written in RStudio and used the following three packages: ade4, readxl, and Mass.

Use of AI tools

An AI-based language model was used solely to assist with English language editing. All revisions were carefully reviewed by the authors to ensure that the scientific meaning was not altered

Data Availability

Processed data are included in the article and Supplementary Information. Additional raw data are available from the corresponding author upon reasonable request.

Code Availability

The data processing and statistical analysis scripts used in this study are provided as Supplementary Information (Supplementary Script 1). The scripts rely on existing open-source packages and were used without modification.

Competing interests

The authors declare no competing interests.

References

1. Goodenough, J. B. & Park, K.-S. The Li-ion rechargeable battery. A perspective. *Journal of the American Chemical Society* **135,** 1167–1176 (2013).
2. Tarascon, J. M. The Li-ion battery. 25 years of exciting and enriching experiences. *The Electrochemical Society Interface* **25,** 79 (2016).
3. Li, M., Lu, J., Chen, Z. & Amine, K. 30 years of lithium-ion batteries. *Advanced Materials* **30,** 1800561 (2018).
4. Wang, J. *et al.* Toward Direct Regeneration of Spent Lithium-Ion Batteries. A Next-Generation Recycling Method. *Chemical Reviews* **124,** 2839–2887 (2024).
5. Zhang, W., Xu, C., He, W., Li, G. & Huang, J. A review on management of spent lithium ion batteries and strategy for resource recycling of all components from them. *Waste Management & Research* **36,** 99–112 (2018).
6. Maisel, F., Neef, C., Marscheider-Weidemann, F. & Nissen, N. F. A forecast on future raw material demand and recycling potential of lithium-ion batteries in electric vehicles. *Resources, Conservation and Recycling* **192,** 106920 (2023).
7. Dolega, P., Bulach, W., Betz, J., Degreif, S. & Buchert, M. Green technologies and critical raw materials. *Strategies for a circular economy, Freiburg/Darmstadt/Berlin* (2021).
8. Helbig, C. & Hillenbrand, M. Principles of a Circular Economy for Batteries. *Emerging Battery Technologies to Boost the Clean Energy Transition*, 13 (2024).

9. Hool, A., Helbig, C. & Wierink, G. Challenges and opportunities of the European critical raw materials act. *Mineral Economics* **37,** 661–668 (2024).
10. Kaya, M. State-of-the-art lithium-ion battery recycling technologies. *Circular Economy* **1,** 100015 (2022).
11. Jiang, S. *et al.* Assessment of end-of-life electric vehicle batteries in China. Future scenarios and economic benefits. *Waste Management* **135,** 70–78 (2021).
12. Dobó, Z., Dinh, T. & Kulcsár, T. A review on recycling of spent lithium-ion batteries. *Energy Reports* **9,** 6362–6395 (2023).
13. Gunarathne, V. *et al.* Hydrometallurgical processes for heavy metals recovery from industrial sludges. *Critical Reviews in Environmental Science and Technology* **52,** 1022–1062 (2022).
14. Roy, J. J. *et al.* Direct recycling of Li-ion batteries from cell to pack level. Challenges and prospects on technology, scalability, sustainability, and economics. *Carbon Energy* **6,** e492 (2024).
15. Charpentier, N. M., Xia, D. & Gabriel, J.-C. P. Printed circuit board recycling. A focus on a novel, efficient and sustainable process for spent critical metals recovery. *Comptes Rendus. Chimie* **27,** 1–11 (2024).
16. Yao, Y. *et al.* Hydrometallurgical processes for recycling spent lithium-ion batteries. A critical review. *ACS Sustainable Chemistry & Engineering* **6,** 13611–13627 (2018).
17. Ahmed, S., Nelson, P. A., Gallagher, K. G., Susarla, N. & Dees, D. W. Cost and energy demand of producing nickel manganese cobalt cathode material for lithium ion batteries. *Journal of Power Sources* **342,** 733–740 (2017).
18. Petzold, M. & Flamme, S. Recycling Strategies for Spent Consumer Lithium-Ion Batteries. *Metals* **14,** 151 (2024).
19. Sziegoleit, H. Sortierung von Gerätebatterien. *Recycling und Rohstoffe* **6,** 495–504 (2013).
20. Shengyu Tao *et al.* Collaborative and privacy-preserving retired battery sorting for profitable direct recycling via federated machine learning.
21. Xu, Z. *et al.* A novel clustering algorithm for grouping and cascade utilization of retired Li-ion batteries. *Journal of Energy Storage* **29,** 101303 (2020).
22. Lai, X., Qiao, D., Zheng, Y. & Yi, W. A novel screening method based on a partially discharging curve using a genetic algorithm and back-propagation model for the cascade utilization of retired lithium-ion batteries. *Electronics* **7,** 399 (2018).
23. Medic, D., Milic, S., Alagic, S., Djordjevic, I. & Dimitrijevic, S. Classification of spent Li-ion batteries based on ICP-OES/X-ray characterization of the cathode materials. *Hem Ind* **74,** 221–230; 10.2298/HEMIND200114012M (2020).
24. Li, X. *et al.* Fast Determination of Lithium Content in Spent Cathodes for Direct Battery Recycling. *Advanced Sustainable Systems* **4**; 10.1002/adsu.202000073 (2020).

25. Charpentier, N. M. *et al.* Urban mining of unexploited spent critical metals from E-waste made possible using advanced sorting. *Resources, Conservation and Recycling* **196,** 107033 (2023).

26. Ferreira, D. S., Pereira, F. M. V., Olivieri, A. C. & Pereira-Filho, E. R. Electronic waste analysis using laser-induced breakdown spectroscopy (LIBS) and X-ray fluorescence (XRF). Critical evaluation of data fusion for the determination of Al, Cu and Fe. *Analytica Chimica Acta* **1303,** 342522 (2024).

27. Soge, A. O., Willoughby, A. A., Dairo, O. F. & Onatoyinbo, O. O. Cathode Materials for Lithium-ion Batteries. A brief review. *Journal of New Materials for Electrochemical Systems* **24** (2021).

28. Zhu, P. *et al.* A review of current collectors for lithium-ion batteries. *Journal of Power Sources* **485,** 229321 (2021).

29. Prasanna, K., Kim, C.-S. & Lee, C. W. Effect of SiO2 coating on polyethylene separator with different stretching ratios for application in lithium ion batteries. *Materials Chemistry and Physics* **146,** 545–550 (2014).

30. Marom, R., Haik, O., Aurbach, D. & Halalay, I. C. Revisiting LiClO4 as an electrolyte for rechargeable lithium-ion batteries. *Journal of the Electrochemical Society* **157,** A972 (2010).

31. Shao, H. *et al.* Modified separators coated with a Ca (OH) 2–carbon framework derived from crab shells for lithium–sulfur batteries. *Journal of Materials Chemistry A* **4,** 16627–16634 (2016).

32. García-López, M. A., Oropeza-Guzmán, M. T. & Calva-Yáñez, J. C. Reclaimed δ-MnO2 from exhausted Zn/C primary cells as active cathode in secondary Zn2+ ion batteries. *Journal of Solid State Electrochemistry* **26,** 2479–2489 (2022).

33. Liang, D. D., Xiang, H. F., Liang, X., Cheng, S. & Chen, C. H. Spinel MgAl 2 O 4 modification on LiCoO 2 cathode materials with the combined advantages of MgO and Al 2 O 3 modifications for high-voltage lithium-ion batteries. *RSC Advances* **7,** 6809–6817 (2017).

34. Rozenblit, A., Torres, W. R., Tesio, A. Y. & Calvo, E. J. Effect of particle size in Li4Ti5O12 (LTO)-LiMn2O4 (LMO) batteries. A numerical simulation study. *Journal of Solid State Electrochemistry* **25,** 2395–2408 (2021).

35. Azhari, L. *et al.* Effects of Extended Aqueous Processing on Structure, Chemistry, and Performance of Polycrystalline LiNi x Mn y Co z O2 Cathode Powders. *ACS applied materials & interfaces* **12,** 57963–57974 (2020).

36. Huang, Y. *et al.* Easily obtaining excellent performance high-voltage LiCoO2 via Pr6O11 modification. *Energy & Environmental Materials* **6,** e12311 (2023).

37. Song, W. *et al.* A systematic study of electrolyte additives in single crystal and bimodal LiNi0. 8Mn0. 1 Co0. 1O2/graphite pouch cells. *Journal of the Electrochemical Society* **168,** 90503 (2021).

Acknowledgments

This work was supported by the European project RESTART (LEAP RE program). The LEAP Re project has received funding from the European Union's Horizon 2020 research and Innovation Program under grant agreement 963530. The authors are grateful to 1001 PILES BATTERIES (Aix-en-Provence, France) for providing the spent batteries. This work benefited from the MATRIX platform (CEREGE, France), funded by the French "Investissements d'Avenir" program managed by the French National Research Agency through Nano-ID (EQUIPEX ANR-10-EQPX39-01) and IMAGINE2 (EQUIPEX ANR-21-ESRE-0043). Matrix is member of the REGEF French research infrastructure.

Author Information

Feihong Ren[1,3], Vladimir Vidal[1], Andréa Campos[2], Florence Vacandio[3], Bernard Angeletti[1], Isabelle Giffard[1], Perrine Chaurand[1], Daniel Borschneck[1], Suanto Syahputra[3], Jérôme Rose[1], Ismael Saadoune[4], Clément Levard[1,*]

Author affiliations :

1 Aix Marseille Univ, CNRS, IRD, INRAE, Coll France, CEREGE, Aix-en-Provence, France

2 Aix Marseille Univ, CNRS, Centrale Marseille, FSCM (FR1739), CP2M, 13397 Marseille, France

3 Aix Marseille Univ, CNRS, MADIREL (UMR 7246) and International Laboratory: Ionomer Materials for Energy, Campus St Jérôme, 13013 Marseille, France

4 Mohammed VI Polytechnic University (UM6P), Lot 660 – Hay Moulay Rachid, 43150 Benguerir, Morocco

Corresponding Author

*Clément Levard

E-mail: levard@cerege.fr ORCiD: 0000-0001-7507-7959

Author contributions

Feihong Ren designed and carried out most of the experiments, collected the end-of-life battery samples, performed data processing, prepared the figures and tables, and wrote and revised the manuscript. Vladimir Vidal, Perrine Chaurand, and Daniel Borschneck provided guidance on the XRF platform and were responsible for its maintenance. Andréa Campos performed the SEM–EDS analyses, contributed to the discussion of the results, and reviewed the manuscript. Florence Vacandio provided guidance on the electrochemical analyses, contributed to the discussion of the results, and reviewed the manuscript. Suanto Syahputra assisted with the electrochemical measurements. Bernard Angeletti and Isabelle Giffard conducted the ICP–OES analyses and processed the corresponding data. Jérôme Rose and Ismael Saadoune contributed to project discussions and manuscript review. Clément Levard supervised the first author, contributed to the experimental design, discussed the results, and reviewed and revised the manuscript.

Ethics Declarations

The authors declare that this study does not involve any human participants, animals, or personal data.

Additional Information

Supplementary information is available for this paper.

Figure Legends

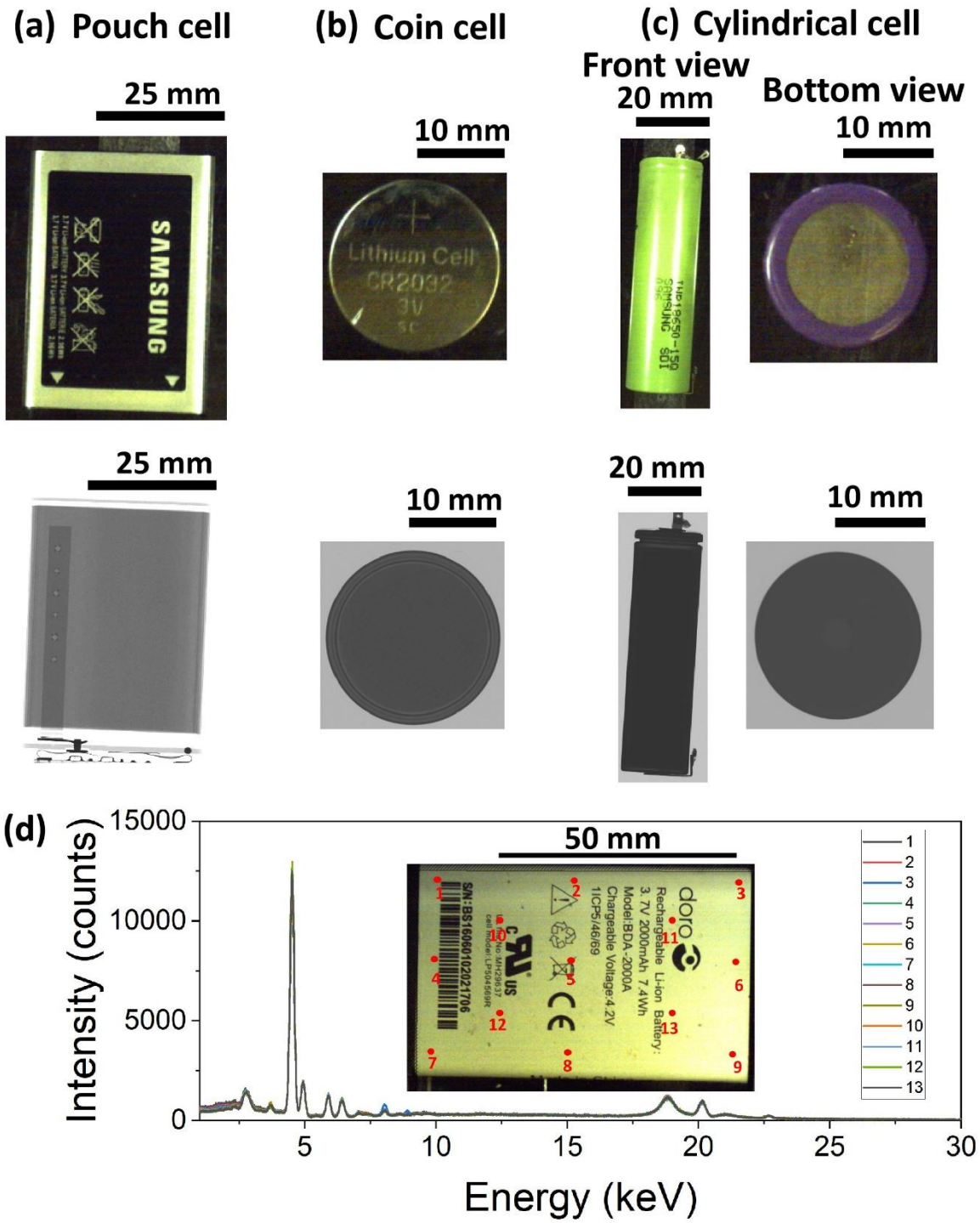

Figure 1. Representative cell formats and XRF measurement configuration. Optical photos and XRT images of (a) pouch cell, (b) coin cell and (c) cylindrical cell (Front view and bottom view); (d) XRF spectra at points on the pouch cell.

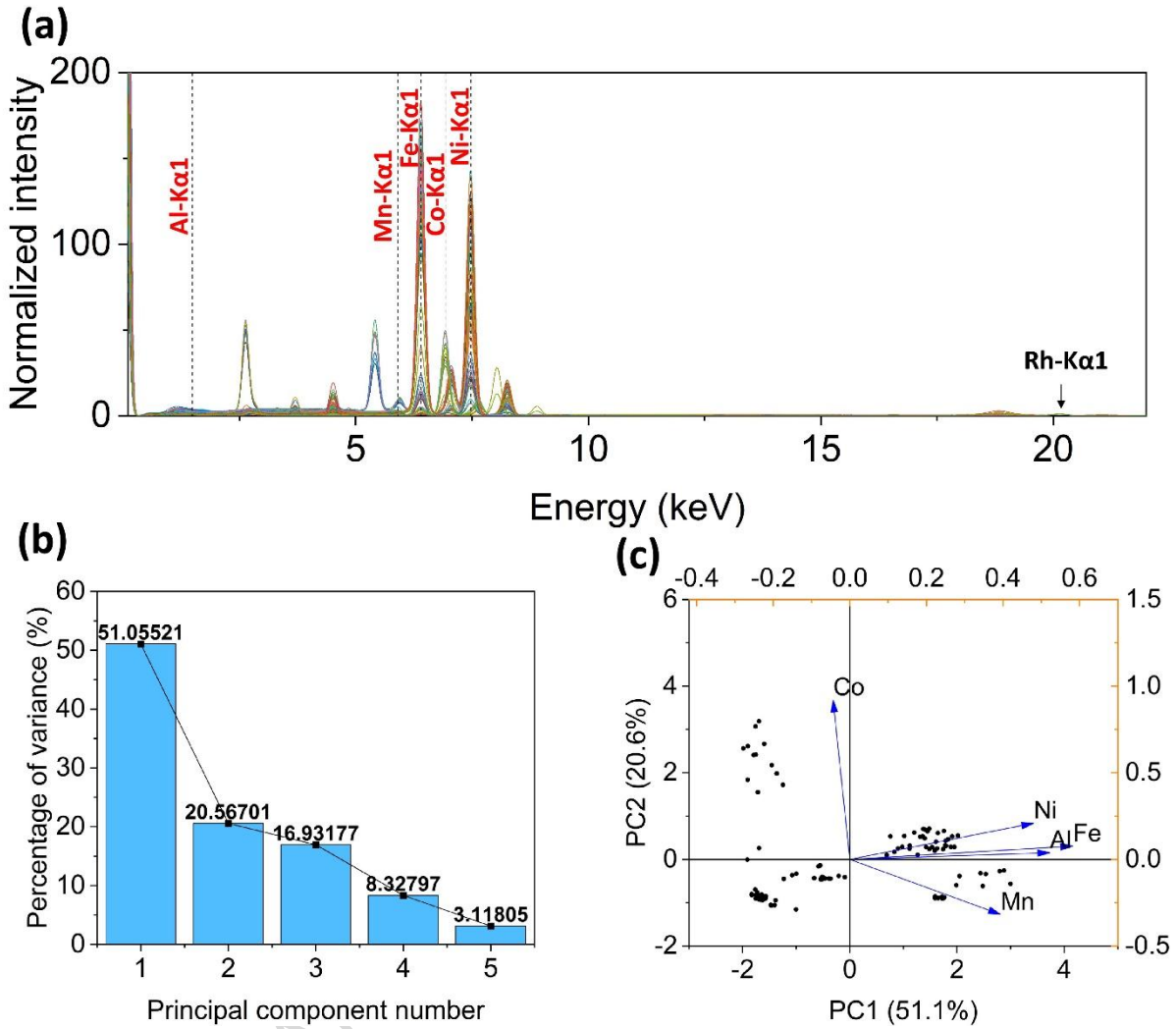

Figures 2. XRF spectra-based PCA from EOL LIBs. (a) Compilation of XRF spectra of 108 batteries (average of spectra from 5 points and normalized by Rh-Kα1); PCA (b) scree plot and (c) biplot of intensities of 5 elemental variables (Al, Mn, Fe, Co, Ni) from XRF spectra obtained from 108 batteries. In Figure 2c, Black points are sample scores on PC1–PC2 (left/bottom axes, in PC score units). Blue arrows are variable loadings plotted on their own normalized axes (right/top); arrow direction indicates how each element varies with the PCs and arrow length reflects its contribution magnitude. The right/top axes therefore report the loading-coordinate scale (dimensionless, normalized) and are not the same units as the score axes.

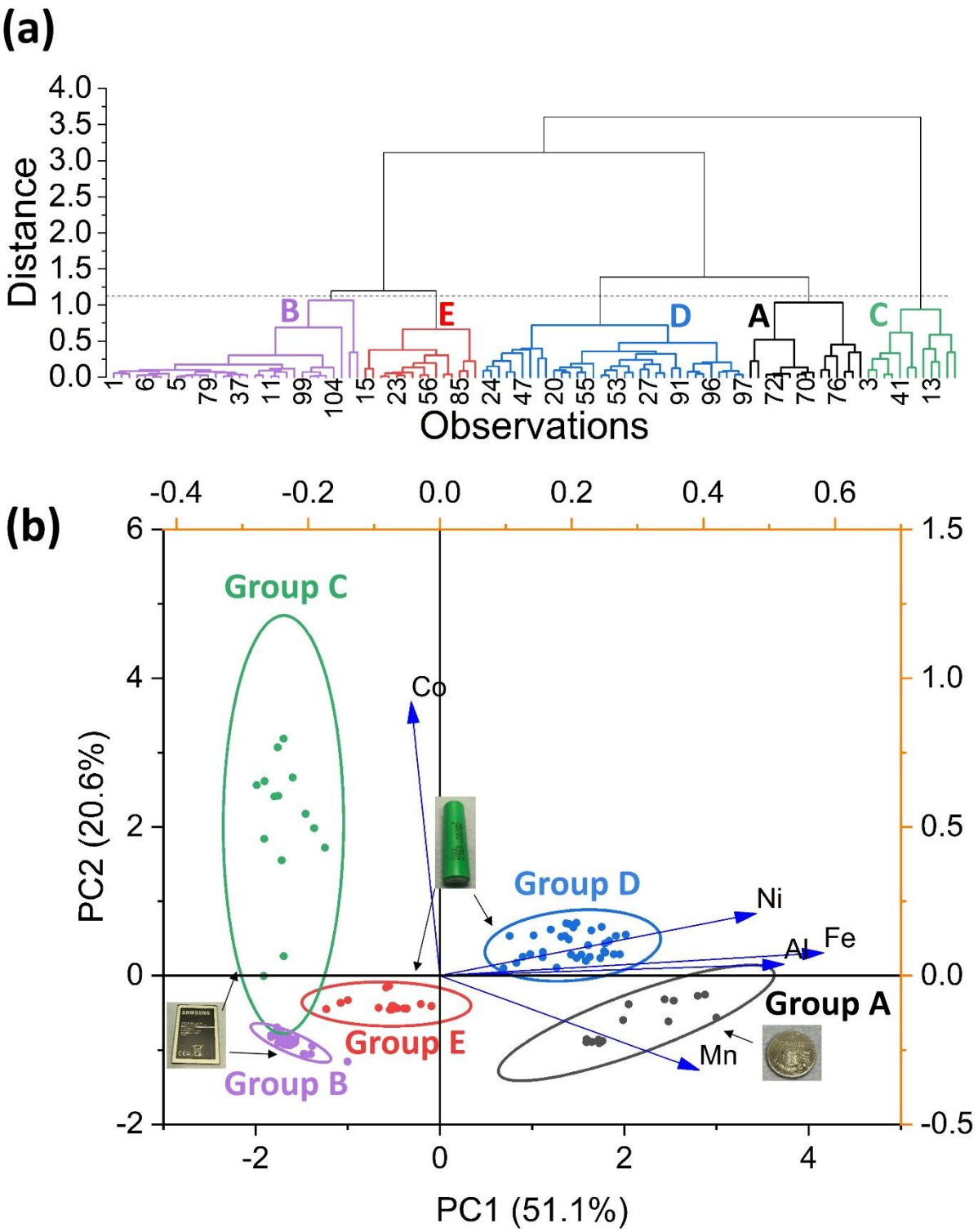

Figure 3. Combined HCA and PCA for battery classification. (a) HCA dendrogram calculated based on PC1 and PC2 (b) enhanced hierarchical cluster PCA biplot. In Figure 3b, colored points

are group scores (A–E) on PC1–PC2 (left/bottom axes). Blue arrows are variable loadings shown on normalized loading axes (right/top), same as Figure 2c.

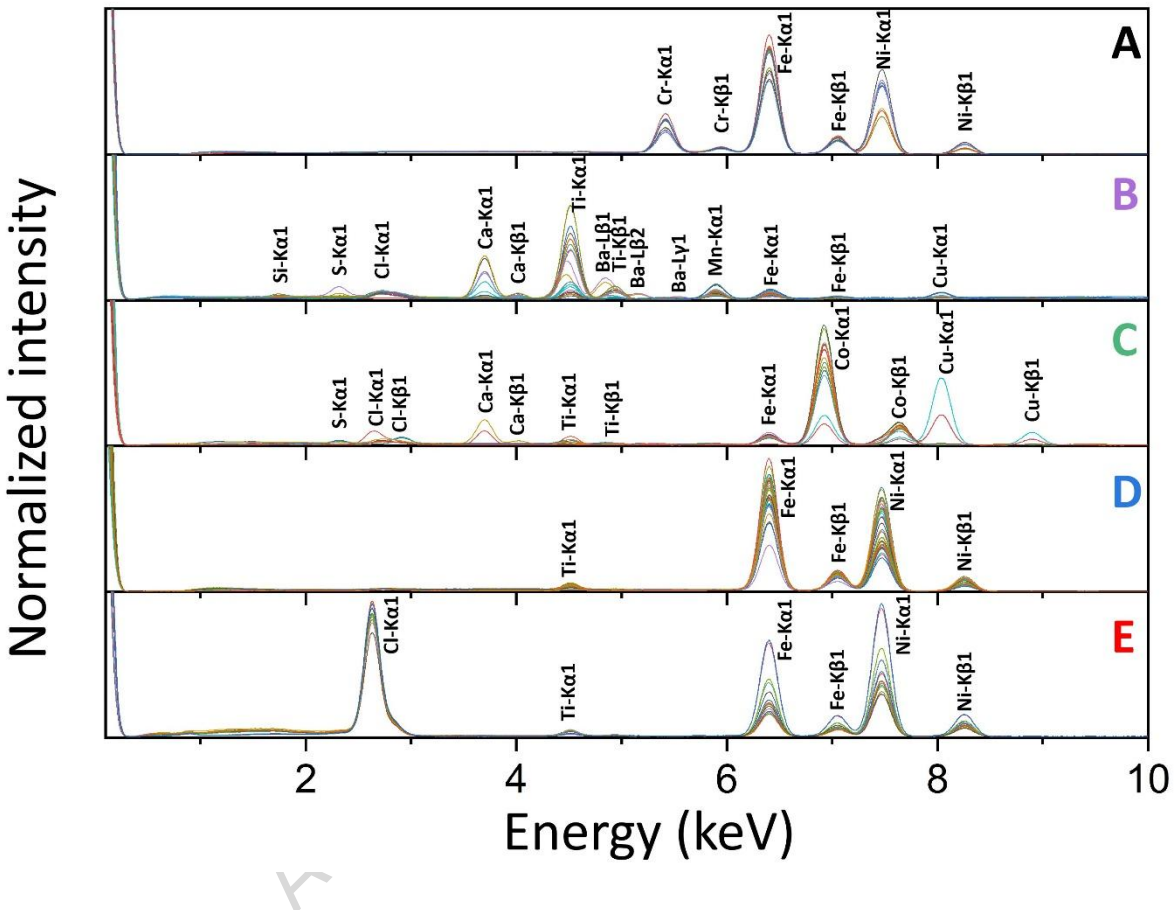

Figure 4. Compilation of XRF spectra of 5 groups derived from HCA and PCA results. Panels (a–e) correspond to groups A–E, respectively, as defined in Table 1.

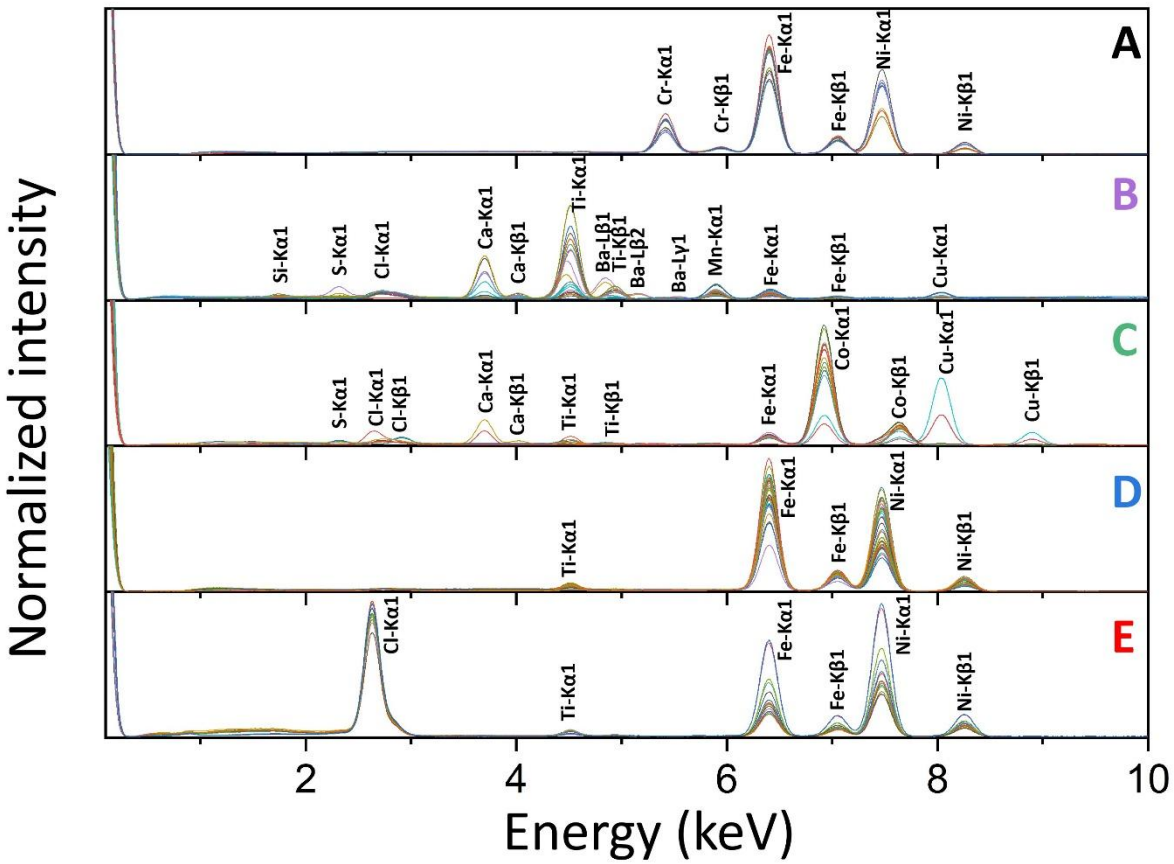

Figure 5. XRF spectra of cathode materials and intact battery obtained from 15 samples in 5 groups (3 samples from each group). Panels (a–e) correspond to groups A–E, respectively, as defined in Table 1. Green labels indicate the elements present in both the cathode and in the intact battery.

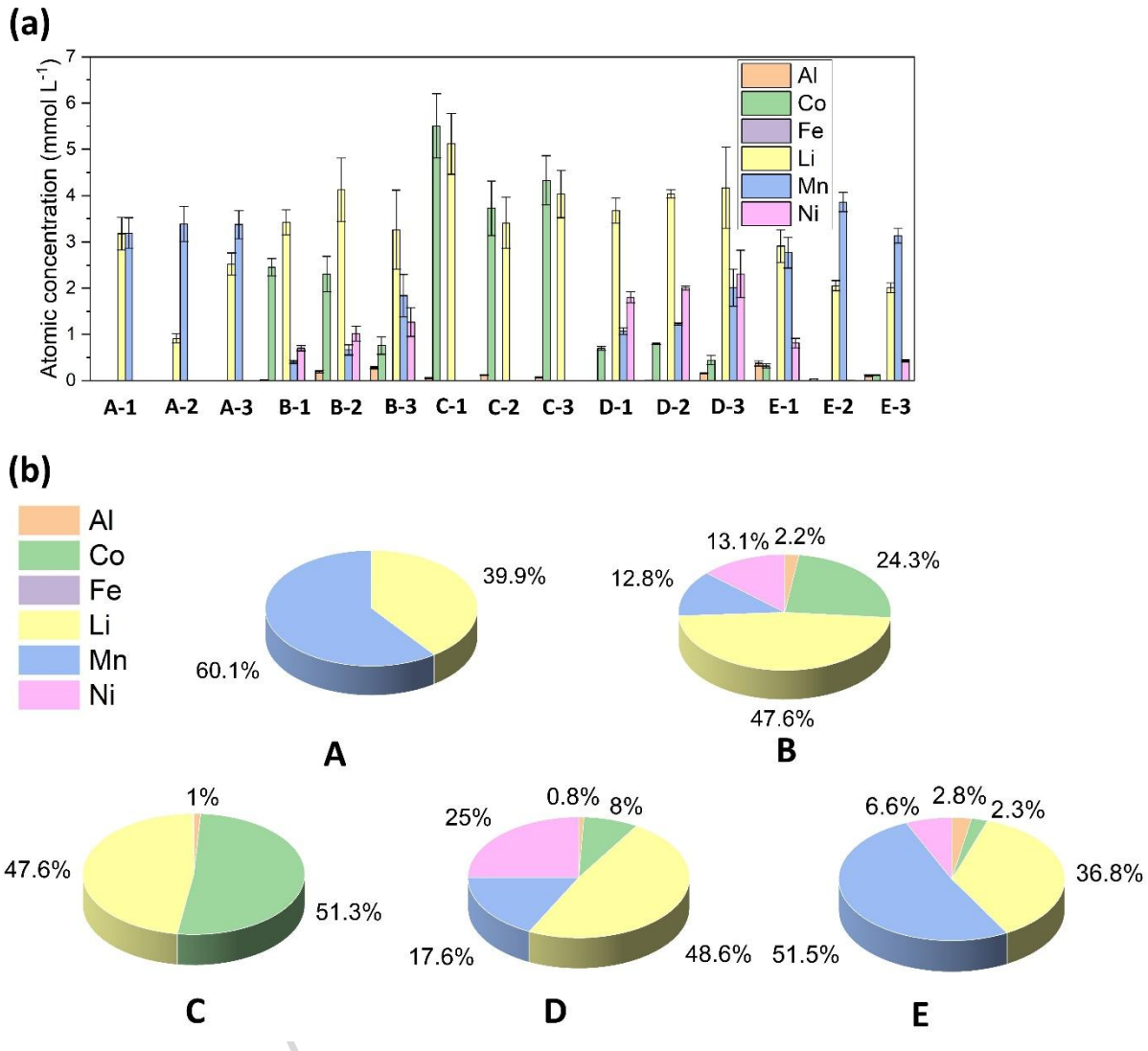

Figure 6. Quantity analysis of ICP-OES: (a) atomic concentration of elements Li, Al, Mn, Fe, Co, and Ni in each group; (b) average atomic concentration of elements in each group. Error bars represent the standard deviation calculated from three independently prepared and measured samples (n = 3).

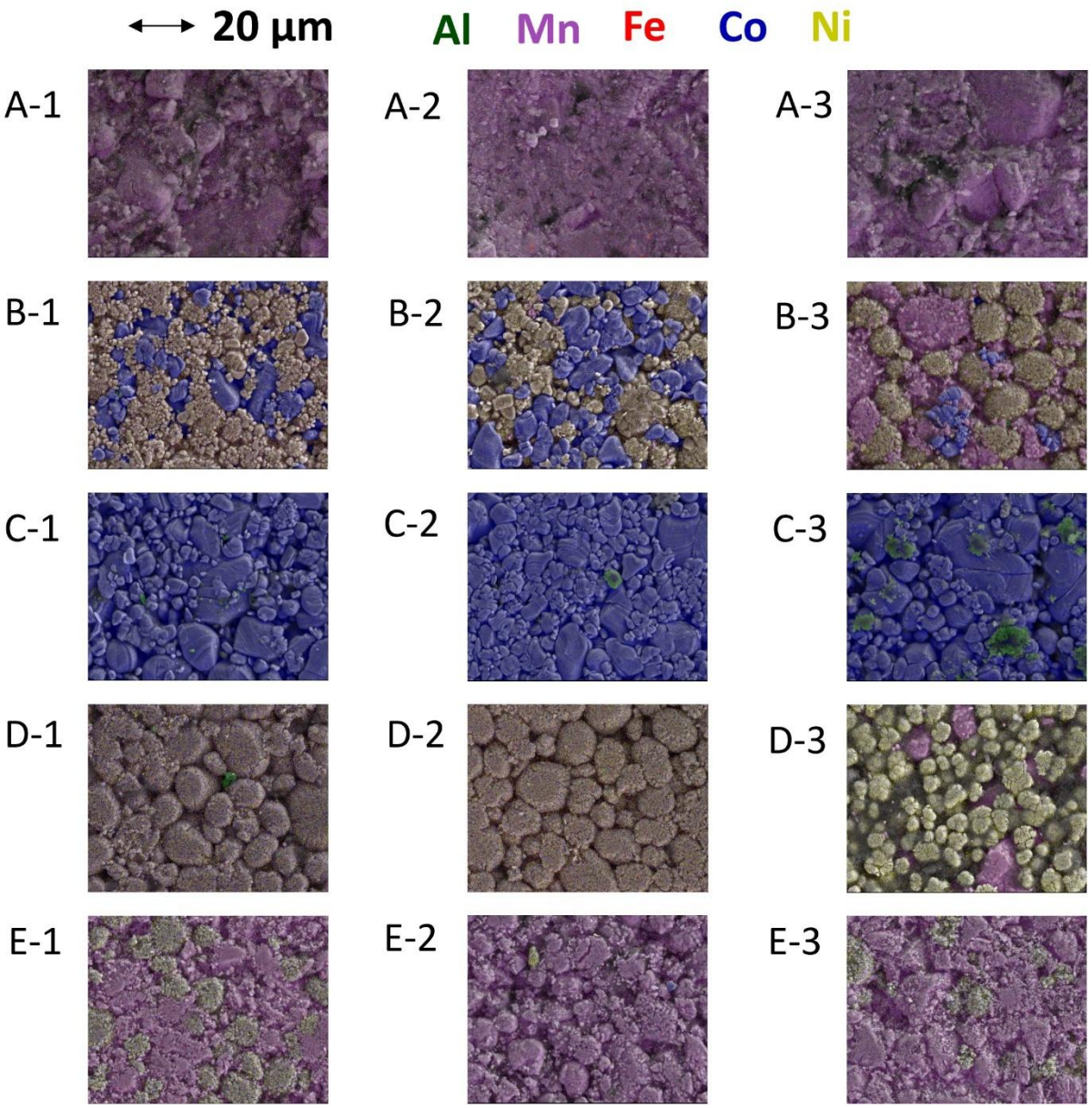

Figure 7. SEM-EDS overlay mapping images of the cathode materials in 15 samples in 5 groups (3 samples from each group). Panels (a–e) correspond to groups A–E, respectively, as defined in Table 1.

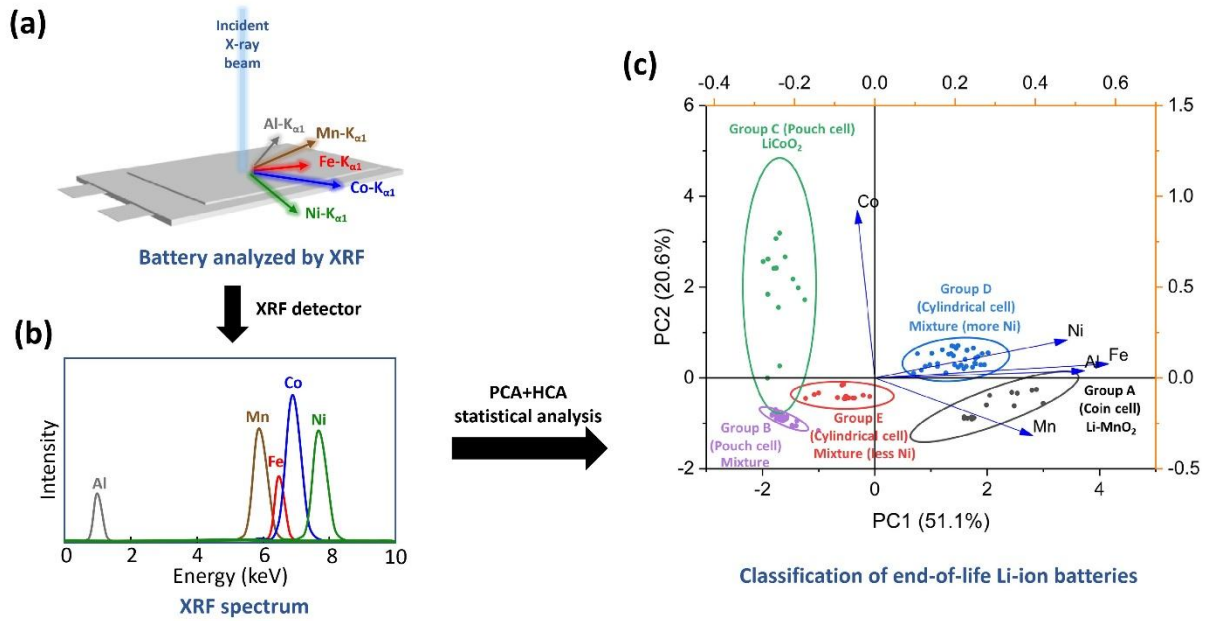

Figure 8. Overview of the XRF-based workflow for classifying EOL LIBs. (a) Schematic illustration of XRF analysis performed directly on intact batteries, showing the detection of characteristic Kα emission lines from metal elements. (b) Schematic XRF spectrum highlighting elemental fingerprints (Al, Mn, Fe, Co, Ni) used for statistical classification. (c) PCA score plot combined with HCA, illustrating the classification of end-of-life lithium-ion batteries into distinct groups according to cathode chemistry and cell format.

Tables

Table 1. Representative battery samples showing the cell type, detected metallic elements (with their $K\alpha_1$ energies for reference), DA-predicted group, validated cathode chemistry, and maximum post probability (P_{max}, ranging from 0 to 1). The predicted group is the one with P_{max} (reported to two decimal places). A higher Pmax indicates a higher confidence that the sample belongs to that group, and the post probabilities of each sample for all five DA groups are summarized in Supplementary Table 11.

Sample code	Cell type	Main metals (Al, Mn, Fe, Co, Ni) detected from intact batteries and their $K_{\alpha 1}$ energies	DA-predicted group	Max post probability (P_{max})	Cathode chemistry (validated by ICP-OES/SEM-EDS)
A-1	Coin cell	Fe (6.40), Ni (7.48)	A	1	Li–MnO_2
A-2	Coin cell	Fe (6.40)	A	1	Li–MnO_2
A-3	Coin cell	Fe (6.40), Ni (7.48)	A	1	Li–MnO_2
B-1	Pouch cell	Mn (5.90), Fe (6.40),	B	1	$LiNi_xCo_yMn_zO_2$, $LiCoO_2$
B-2	Pouch cell	Mn (5.90), Fe (6.40),	B	1	$LiNi_xCo_yMn_zO_2$, $LiCoO_2$
B-3	Pouch cell	Mn (5.90), Fe (6.40),	B	0.99	$LiNi_xCo_yMn_zO_2$, $LiCoO_2$, $LiMn_2O_4$
C-1	Pouch cell	Fe (6.40), Co (6.93)	C	1	$LiCoO_2$
C-2	Pouch cell	Fe (6.40), Co (6.93)	C	1	$LiCoO_2$
C-3	Pouch cell	Fe (6.40), Co (6.93)	C	1	$LiCoO_2$
D-1	Cylindrical cell	Fe (6.40), Ni (7.48)	D	1	$LiNi_xCo_yMn_zO_2$
D-2	Cylindrical cell	Fe (6.40), Ni (7.48)	D	1	$LiNi_xCo_yMn_zO_2$
D-3	Cylindrical cell	Fe (6.40), Ni (7.48)	D	0.99	$LiNi_xCo_yMn_zO_2$, $LiMn_2O_4$
E-1	Cylindrical cell	Fe (6.40), Ni (7.48)	E	0.99	$LiNi_xCo_yMn_zO_2$, $LiMn_2O_4$

E-2	Cylindrical cell	Fe (6.40), Ni (7.48)	E	1	$LiMn_2O_4$
E-3	Cylindrical cell	Fe (6.40), Ni (7.48)	E	1	$LiNi_xCo_yMn_zO_2$, $LiMn_2O_4$

Editor's Summary:

Feihong Ren and colleagues report a rapid X-ray fluorescence–based method to identify the cathode chemistry of end-of-life lithium-ion batteries. This approach enables fast, non-destructive sorting and supports more efficient battery recycling.

Peer review information:
Communications Engineering thanks Jiadong Yu, Misaki Katayama and Joseph Jegan Roy for their contribution to the peer review of this work. Primary Handling Editors: [Jiangong Zhu] and [Rosamund Daw]. A peer review file is available.